

Grain orientation dependence of the forward and reverse fcc ↔ hcp transformation in FeMnSi-based shape memory alloys studied by *in situ* neutron diffraction

A. Arabi-Hashemi¹, E. Polatidis², M. Smid^{3,4}, T. Panzner², C. Leinenbach¹

¹Empa, Swiss Federal Laboratories for Materials Science and Technology, Überlandstr. 129, 8600 Dübendorf, Switzerland

²Laboratory for Neutron Scattering and Imaging, Paul-Scherrer-Institute, 5232 Villigen PSI, Switzerland

³Swiss Light Source, Paul Scherrer Institute, 5232 Villigen PSI, Switzerland

⁴Institute of Physics of Materials, Czech Academy of Sciences, 616 62 Brno, Czech Republic

Abstract

The grain orientation dependence of the deformation-induced forward fcc→hcp and reverse hcp→fcc martensite transformation of a FeMnSi-based shape memory alloy was studied by *in situ* neutron diffraction during cyclic loading. A deformation-induced fcc→hcp transformation is observed during tensile straining to +2%. The hcp martensite phase that forms under tension partially reverts to fcc austenite upon subsequent compression from +2% → -2% for the {220}, {331} and {111} grain families aligned with respect to the loading direction but not for the {200} grain family. The martensite formation and the reversion of the individual grains can be explained by considering grain orientation dependent Schmid factors of the {111}<112> slip system underlying the fcc to hcp transformation. While for post-yield elastically compliant grains the Schmid factor of the leading partial dislocation is larger than that of the trailing partial dislocation, the opposite is true for post-yield elastically stiff grains. The former grains show a phase reversion, i.e. hcp→fcc upon compression, the latter grains do not transform back to fcc. EBSD characterization confirms the phase reversion for a <541> orientated grain by the disappearance of hcp bands. Martensite bands, which have not reverted to austenite during compression, showed a thickening. The thickening of existing bands during compression is associated with the activation of a second slip system.

Keywords

FeMnSi, Neutron diffraction, martensite transformation, Schmid factor

This document is the accepted manuscript version of the following article:
Arabi-Hashemi, A., Polatidis, E., Smid, M., Panzner, T., & Leinenbach, C. (2020). Grain orientation dependence of the forward and reverse fcc ↔ hcp transformation in FeMnSi-based shape memory alloys studied by *in situ* neutron diffraction. *Materials Science and Engineering A: Structural Materials: Properties, Microstructure and Processing*, 782, 139261 (11 pp.).
<https://doi.org/10.1016/j.msea.2020.139261>

This manuscript version is made available under the CC-BY-NC-ND 4.0 license <http://creativecommons.org/licenses/by-nc-nd/4.0/>

1 Introduction

The shape memory effect (SME) in FeMnSi-based alloys was first discovered by Sato in the 1980ies [1,2]. The SME in FeMnSi-based alloys is based on the deformation-induced transformation from the parent face-centered cubic (fcc) phase into the hexagonal-closed packed (hcp) phase and its reversion upon heating. The mechanism of the fcc→hcp transformation is similar to deformation twinning in the fcc crystal structure: the fcc lattice can be transformed into a hcp lattice by the formation of partial dislocations separated by stacking faults on every second {111} layer while a deformation twin is formed by stacking faults on every subsequent {111} layer. If a tensile load is changed into compressive, the phase transformation can be reverted (hcp→fcc) or a twin can be de-twinned. The fcc→hcp transformation is usually observed in alloys with stacking fault energies $<20 \text{ mJ/m}^2$ [3–5], whereas deformation twinning is observed for higher stacking fault energies between $20 - 40 \text{ mJ/m}^2$ [6,7].

Compared to the most widely studied shape memory alloy (SMA) NiTi, FeMnSi-based SMAs have the advantage of low material and manufacturing costs. The combination of low costs and the unique thermo-mechanical behavior triggered extensive research of the alloy system for the last four decades. Significant efforts have been made to increase the SME by optimizing e.g. the chemical composition [1,8], introducing thermo-mechanical treatments [9,10] and the formation of precipitates [11]. By using carbide- or nitride-based precipitates an almost perfect SME in polycrystalline FeMnSi-based shape memory alloys was achieved for strains up to around 4% without the need of training [11]. In the recent years, FeMnSi-based SMAs were considered for various applications such as pre-stressing of concrete structures for civil engineering [12–14], clamping and coupling [15,16], and also seismic damping [17,18]. In all these applications, the FeMnSi-based SMA might be subject to cyclic loading and is thus prone to fatigue failure. It has been shown that in comparison with steels, FeMnSi-based SMA exhibit excellent low cycle fatigue properties which is attributed to the reversible $\text{fcc} \leftrightarrow \text{hcp}$ transformation [19]. The low cycle fatigue properties of FeMnSi-based alloys were improved recently by modifying the alloy composition so that a high degree of reversibility $\text{fcc} \leftrightarrow \text{hcp}$ and a high yield strength were achieved at the same time [20–22]. Another way to improve the low cycle fatigue properties would be to modify and select the texture of the material in a favorable way. For this, the impact of grain orientation on the deformation induced forward and reverse $\text{fcc} \leftrightarrow \text{hcp}$ transformation must be known. A detailed understanding of the forward $\text{fcc} \rightarrow \text{hcp}$ and reverse $\text{hcp} \rightarrow \text{fcc}$ phase transformation and its grain orientation dependence is thus of particular interest, but while detwinning in fcc crystals has been frequently studied [23,24], the phase reversion for the $\text{fcc} \rightarrow \text{hcp}$ is not well understood up to now. The deformation-induced phase reversion $\text{hcp} \rightarrow \text{fcc}$ was evidenced by atomic force microscopy by the appearance and disappearance of the surface relief [25]. However, in the latter study the impact of the grain orientation on the phase reversion was not studied. There is a significant impact of the grain orientation on the forward phase transformation $\text{fcc} \rightarrow \text{hcp}$ [26] and thus it can be expected that the grain orientation also has an impact on the phase reversion $\text{hcp} \rightarrow \text{fcc}$. Recently, Lee et al. investigated twinning-detwinning in gold nanowires and explained this phenomenon with the grain orientation dependence of the Schmid factor (SF) for the leading partial dislocation and the trailing partial dislocation under tension and compression [27]. The effect of grain orientation with respect to the loading

direction has been shown to affect the SF of the leading partial dislocation and the trailing partial dislocation and the associated TRIP [7,28] and TWIP mechanisms [29]. While the tension-compression asymmetry for the fcc-hcp transformation is already studied in detail for sole tension or compression experiments [30], the grain orientation dependent behavior of the fcc-hcp transformation in FeMnSi-based SMAs during a tension-compression cycle has not been studied so far.

Neutron diffraction is a unique method to study the deformation mechanism of a statistically large number of grains due to the high penetration depths of neutrons in metals and the associated large interaction volume. In the past, the fcc→hcp transformation in FeMnSi-based SMAs during static loading was studied by *in situ* neutron diffraction [26,31–33]. However, in none of these studies, the deformation-induced phase reversion hcp→fcc nor any cyclic loading including tension and compression was studied. Recently, a neutron diffraction study during a tension-compression cycle of a TWIP steel gave insights into the grain orientation dependence of twinning and detwinning [24]. It was found that the grain orientation has an impact on whether detwinning takes place.

In the present study the impact of grain orientation on the deformation-induced forward (fcc→hcp) and reverse (hcp→fcc) phase transformation behavior in FeMnSi-based shape memory alloys is studied in detail by employing *in situ* neutron diffraction during a tension-compression cycle. To complement the *in situ* neutron diffraction tests, the electron backscatter diffraction (EBSD) was undertaken at the unloaded state after reaching the maximum loads (both tension and compression). The presented EBSD study allows assessing the deformation behavior, the activation of martensite variants and the reversion of the transformation upon the tension-compression cycle for individual grain orientations.

2 Materials and Methods

Material

An Fe-based shape memory alloy with a nominal composition of Fe₁₇Mn₅Si₁₀Cr₄Ni_{0.75}V_{0.25}C was used. The material was induction melted in air and hot rolled. Subsequently, the alloy underwent solution treatment for 2h at 1130°C to dissolve precipitates and water quenching to receive a fully austenitic microstructure. Finally, the material was aged for 2h at 850°C in a vacuum furnace in order to create carbide-based precipitates.

In situ neutron diffraction during deformation

All tests were done on the uniaxial deformation rig of the time-of-flight diffractometer instrument POLDI of the Swiss spallation source, SINQ at the Paul Scherrer Institute (PSI). For these tests cylindrical specimens with a gauge length of 15mm and a diameter of 6mm were prepared. The extensometer length was 8mm. A M12x1 fine thread was used in order to minimize slip of the sample in the gripping system during the change from tensile to compressive stresses. The strain rate was 0.0067s⁻¹.

Prior to *in situ* neutron diffraction tests, an initial *ex situ* deformation test was performed for the deformation cycle of interest 0% (unstrained) → +2% (tension) → -2% (compression) → 0N (unloading) in order to identify position of test interruptions at which neutron diffraction patterns should be acquired (Figure 1 a)). For this purpose 23 interruptions at certain strain values were selected. All stresses and strains reported in this paper are engineering stresses and strains.

The *in situ* neutron diffraction during the mechanical tests were undertaken by holding the displacement and allowing stress to relax, as shown in Figure 1 a) [34,35]. The first 8 *strains* are situated in the tensile region (0% → +2%). During *strains* 9 to 12 the sample was unloaded from +2% back to 0N load. During *strains* 13 to 20 the sample was compressed to -2%. During *strains* 21 to 23 the sample was unloaded from -2% back to 0N load.

The POLDI instrument has one detector bank at a scattering angle of 90° relative to the incident neutron beam. The loading direction of the dogbone sample was parallel to the scattering vector. The acquisition time varied between 1h, 2h to 2.5h per pattern. The acquisition time was increased during the measurement to obtain good signal to noise ratios for all patterns. The neutron diffraction data were reduced and fitted using the open source software Mantid [36].

EBSD

Quasi *in situ* EBSD mapping was carried out at the same area after loading to two different strain levels: +2% and -2%. For this purpose, a cylindrical tensile sample was strained to +2% and unloaded. A section of the gauge length was cut out of the tensile sample and one side, parallel to the loading direction, was flattened by mechanical grinding with 600, 1200, 2500 and 4000 grit SiC paper and electrochemically polished for 10s with a 16:3:1 (by volume) ethanol, glycerol and perchloric acid solution at 48 V. The first EBSD characterization was taken assessing the effect of tensile loading. The cylinder

was then compressed to -2% and unloaded again followed by EBSD characterization on the same polished surface. A field emission gun scanning electron microstructure (FEG SEM) Zeiss ULTRA 55 equipped with EDAX Hikari Camera operated at 20 kV in high current mode with 120 μm aperture was used. The acquired EBSD raw data were post processed using the EDAX OIM Analysis 7.3 software.

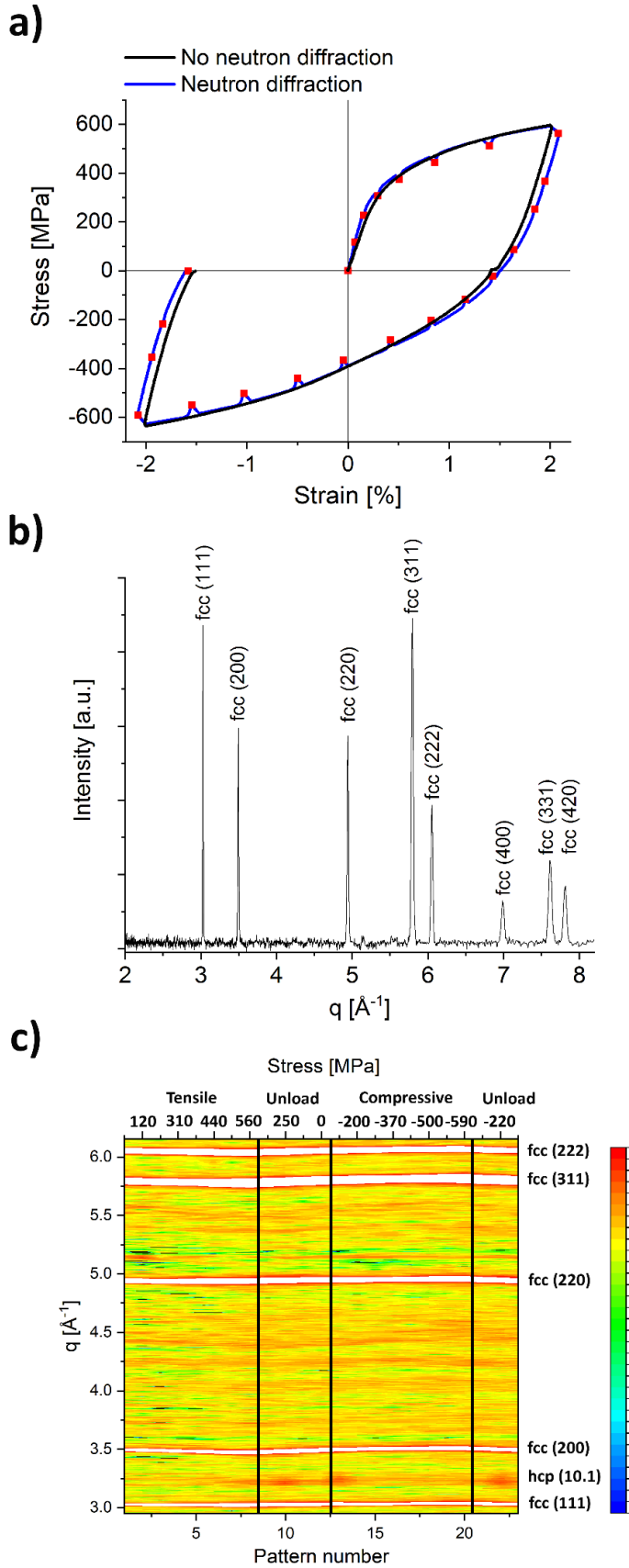


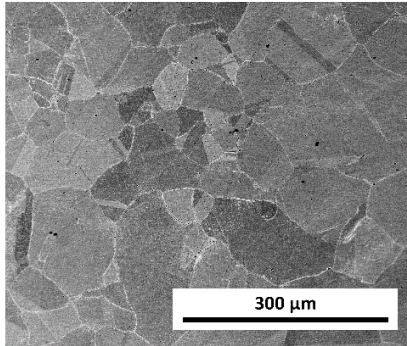
Figure 1: a) Engineering stress-strain curve of a continuous *ex situ* test (black curve) prior to neutron diffraction to identify strains at which neutron diffraction patterns would be acquired. The *in situ* test curve is shown in blue and the red squares show the 23 strains at which neutron diffraction patterns were acquired. b) A neutron diffraction pattern is exemplarily shown for 0% strain. c) Contour plot of all 23 diffraction patterns showing the intensity in logarithmic scale in arbitrary units.

3 Results and discussion

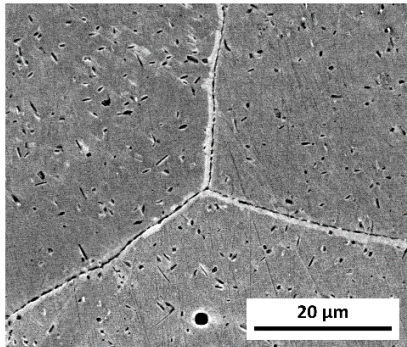
3.1 Microstructure

The microstructure of the FeMnSi-based SMA before and after completing the full load cycle is shown in Figure 2. The material has a coarse grain structure with an area weighted grain size in the range of 100 μm , which formed due to recrystallization during the solution treatment. EBSD characterization revealed a nearly-random initial crystallographic texture for the as-prepared sample. The precipitates which formed after subsequent aging for 2h at 850°C can be seen as dark spots in the backscattered electrons micrograph shown in Figure 2 b). The precipitates are larger than 50 nm and are thus expected to improve the shape memory effect [37]. The material contained VC-based precipitates due to the nominal materials composition containing 0.75 wt. % V and 0.25 wt. % C [38].

a)



b)



c)

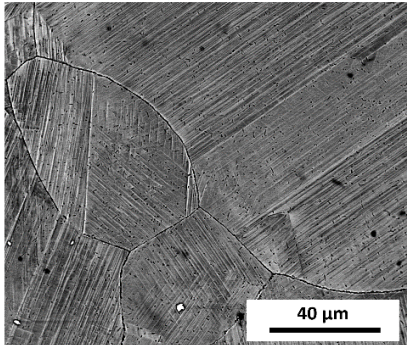


Figure 2: Electron backscatter micrographs of the undeformed sample a) revealing the austenitic grains and b) showing the carbide precipitates. c) After the full deformation cycle at the unloaded state, deformation bands are visible on the surface. Parallel bands are visible for most of the grains indicating strain accommodation by slip and/or hcp variants with the same orientation.

The neutron diffraction pattern shown in Figure 1 b) reveals a fully austenitic material prior to loading. This is in agreement with the absence of martensite bands observed by SEM in Figure 2 a) and b). The neutron diffraction pattern shows 6 hkl-diffraction peaks which are originating from the {111}, {200}, {220}, {311}, {331} and {420} grain families; these grain families have their corresponding hkl-direction parallel to the scattering vector, which is parallel to the loading direction. At around +2% tensile strain, the hcp phase can be identified by the appearance of the (10.1) hcp peak (Figure 1 c)). Compared to the thermally induced martensite transformation, where untextured hcp martensite is formed below the martensite start transformation temperature M_s , the deformation-induced hcp martensite is assumed to be highly textured. The origin of texture is the preferred activation of slip systems with underlying high SF. The hcp martensite is barely seen in the diffraction pattern (Figure 1 c)), which can be due to the following reasons: strong texture in the deformation-induced martensite, low phase fraction of hcp martensite with respect to the neutron diffraction detection limit and low multiplicity of the hcp crystal structure which results in diffraction peaks with (significantly) lower intensity than the parent fcc phase. Therefore, in order to investigate the fcc \leftrightarrow hcp transformation in the present study, changes of the normalized integrated intensities of the austenite phase were analyzed rather than changes of the normalized integrated intensities of hcp peaks.

Under tensile loads, the peaks are shifted to smaller diffraction vectors, while for compressive loads peaks are shifted to larger diffraction vectors as can be seen in Figure 1 c). This behavior is expected since tensile loads increase the lattice spacing of the planes that are fulfilling the Bragg condition and compressive loads will decrease the lattice spacing.

Figure 2 c) shows a SEM micrograph of the sample after the whole deformation cycle in the unloaded state. Every grain of the material showed distinct traces on the surface which are deformation bands of activated slip along one of the {111} planes and are expected to contain hcp phase. In addition, for most of the grains the primary slip plane is active and only a few grains underwent the activation of a slip system on a second plane.

3.2 *In situ* neutron diffraction

3.2.1 Lattice strain vs. stress – elastically compliant and elastically stiff grains

The analysis of the lattice strains as a function of the applied stress reveals two different classes of grain families i) post-yield elastically compliant (PYEC) and ii) post-yield elastically stiff (PYES). In Figure 3, the elastic strains of the PYEC grain families ((a), b) and c)) and the PYES grain families ((d), e) and f)) are plotted against the applied stress. Four different regions are identified: i) A tensile region (0 MPa \rightarrow 560 MPa), ii) unloading (560 MPa \rightarrow 0 MPa), iii) a compressive region (0 MPa \rightarrow -590 MPa) and iv) unloading -590 MPa \rightarrow 0 MPa. The yield stress of 228 MPa is directly obtained from the stress-strain curve as evident from the linear response of the lattice strain versus the applied stress. Each grain family shows a unique plastic behavior. For stresses above 228 MPa, post-yield, the {111}, {220} and {331} grain families start to behave elastically compliant, which means that these grains carry lower elastic strains than expected from the extrapolation of the linear elastic behavior and deform plastically (insets of Figure 3 a), b) and c)). The {220} grain family shows the most pronounced elastically compliant behavior. For stresses above 228 MPa, almost no change of the elastic strain for the {220} grain family

is observed as shown in Figure 3 a). It can be concluded that the {220} grain family deforms fully plastically and does not carry any further elastic strain upon yielding. A similar behavior is observed for the {111} grain family, however these grains do not deform fully plastically, but show a slight increase of elastic strain post-yield. Due to the elastically compliant behavior of the {220}, {111} and {331} grain families, it can be expected that other grains behave elastically stiff and carry the load shed by the PYEC grains. The PYES {200}, {311} and {420} grain families are shown in Figure 3 d), e) and f). These grains carry more load post-yield than based on the extrapolation of the elastic behavior (see insets of Figure 3 d), e) and f).

The applicability of the Schmid law for austenitic steels undergoing the fcc→hcp phase transformation was confirmed in the past [30,39]. During the fcc→hcp transformation the {111}<112> slip system is involved. Due to the unidirectionality of this slip system, the SF for each grain is different for tension and compression [40,41]. The SF for tension and compression for all six grain families are summarized in Table 1. The observed phenomenon of load transfer can be explained by considering the SF of the fcc to hcp phase transformation. The fcc→hcp transformation is associated with the movement of partial dislocations, leading to the formation of stacking faults. It was shown that stacking faults are present in all grains after the aging treatment [38]. It is assumed that these stacking faults are created during cooling from 850°C to room temperature due to stresses caused by the different thermal expansion of the matrix and the carbide precipitates. The equilibrium separation distance of the partial dislocation, the stacking fault width, increases or decreases upon application of an external load. An increase of the stacking fault width takes place when the SF of the leading partial dislocation is larger than the SF of the trailing partial dislocation which is the case for all PYEC {111}, {220} and {331} grain families [42]. For all these grain families, the leading partial dislocation has a SF that is almost twice the value of that for the trailing partial dislocation (Supplementary table). For PYEC grains during tension, the width of the existing stacking faults will increase. For these grains, it is expected that small hcp plates form in the beginning of straining by the overlapping of existing stacking faults in the materials. On the other hand, for the PYES grains the opposite behavior is observed. The SF of the leading partial dislocation is smaller or has the same value than the SF of the trailing partial dislocation. For the {311} and {420} grain families the leading partial dislocations and trailing partial dislocations have same SF while for the {200} grain families the trailing partial dislocations have two times the value of the leading partial dislocations. For the PYES grains, the width of the stacking faults decreases or stays constant. Pre-existing stacking faults act as nucleation sites for the hcp phase as it was observed by transmission electron microscopy [43]. For the {111}, {220} and {331} grain families the formation of hcp phase is facilitated due to the increase of stacking fault width, increasing the availability of nucleation sites. Based on these findings we conclude that grains behave PYEC when the SF of the leading partial dislocation is larger than the SF of the trailing partial dislocation. Grain families, which fulfill this, are presented in an inverse pole figure shown in Figure 6 e).

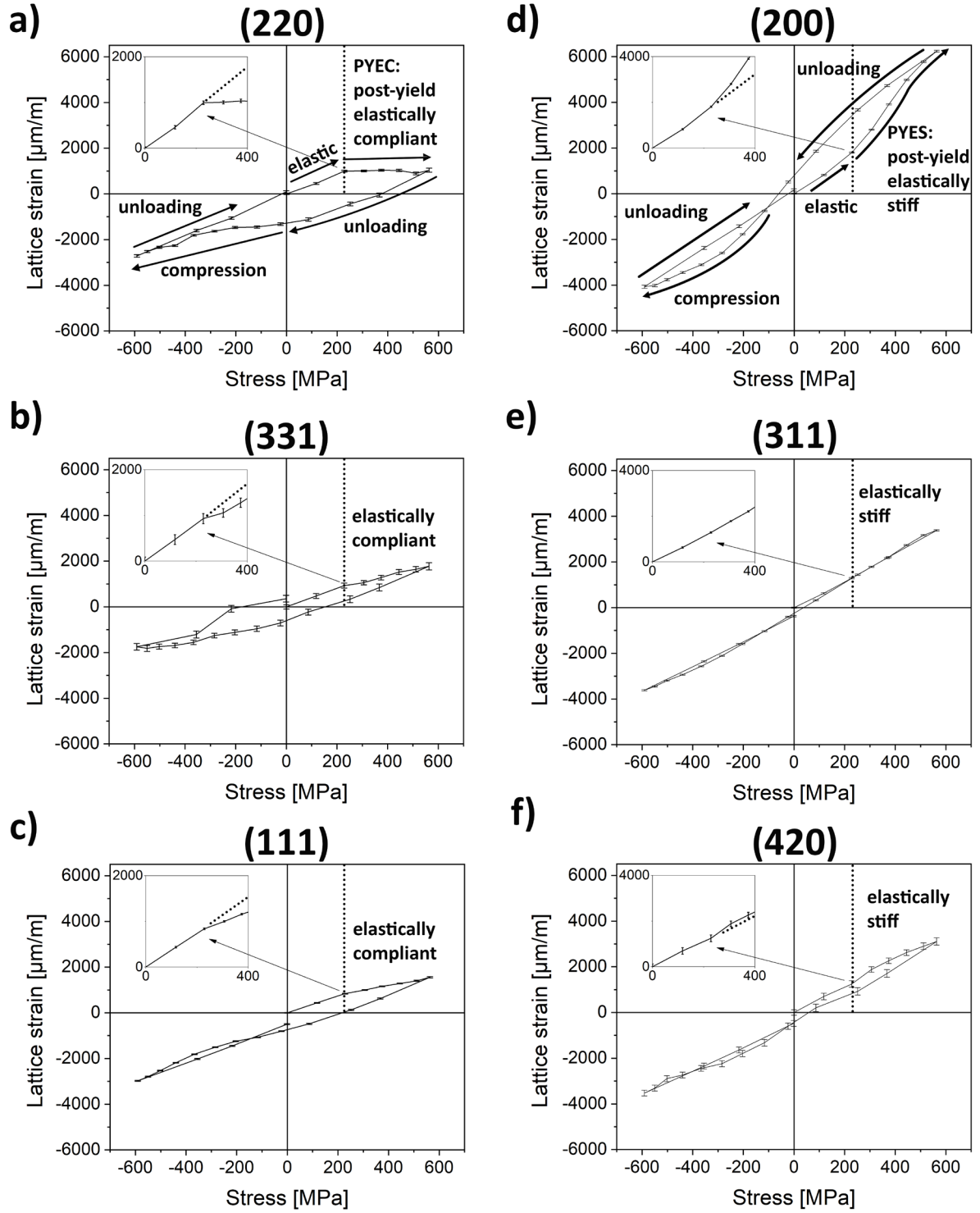


Figure 3: Elastic lattice strain vs. stress for a), b) and c) PYEC grains (mainly plastically deforming in tension) and d), e) and f) PYES grains. The {220} and {200} grain families show the most pronounced elastically compliant and stiff behavior, respectively. The inset shows the stress-strain behavior in the vicinity of the yield stress. The dotted line in the inset is an extrapolation of the linear elastic behavior. For PYEC grains the strain-stress curve is found below the dotted line. The yield stress of around 228 MPa is indicated by a vertical dotted line.

3.2.1 FWHM vs stress – reversion of defects

During tensile loading, the FWHM increases for all grains indicating that the plasticity is governed by an increase of the defect density as shown in Figure 4. In the present case, these defects are partial dislocations related to stacking faults and to the hcp phase. The FWHM decreases during subsequent unloading. This decrease is more pronounced for the PYEC {220}, {331} and {111} grains families than for the PYES {200}, {311} and {420} grain families. Upon compression, the FWHM decreases for all grain families while exhibiting a minimum of the FWHM in the compressive region at a stress range of around -300 to -400 MPa. Upon further compression, the FWHM starts to increase again. It is generally assumed that the FWHM is governed by the defect density of the material. The reversible behavior of the FWHM during compression indicates that the fraction of stacking faults or hcp phase fraction decreases while upon further compression the fraction of stacking faults or hcp phase increases again. This results in a "U"-shape of the FWHM as a function of the applied stress for all grains during compression.

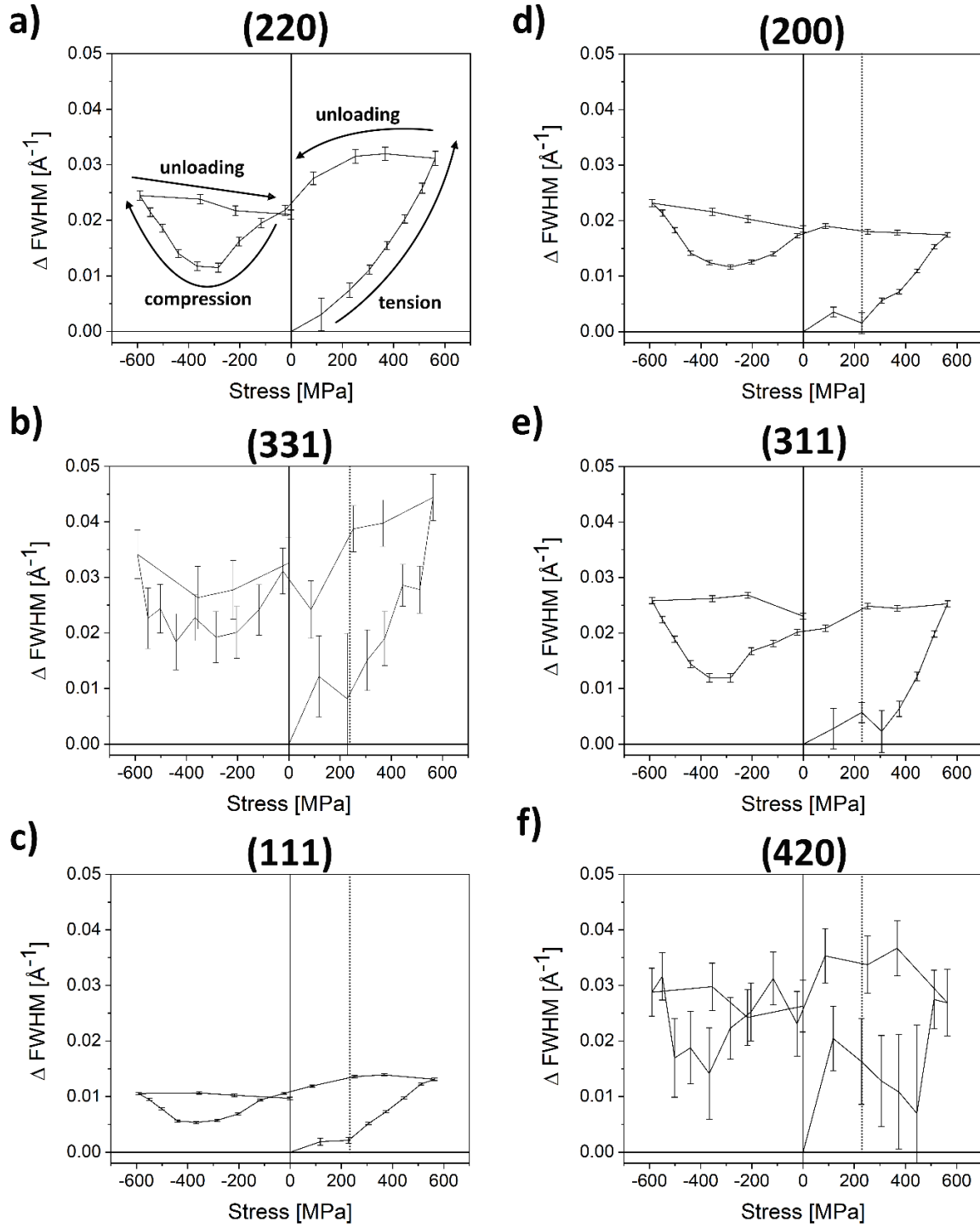


Figure 4: The changes of the FWHM against the applied stress are shown for a), b) and c) PYEC grains and d), e) and f) PYES grains. The loading path is exemplarily shown for the {220} grain families. The FWHM increases during tensile straining. It decreases during unloading and further decreases during compression until a minimum turning point is reached. Upon further compression, the FWHM increases again. The “U” shape behavior in the compressive part of the path is observed for all grains families.

3.2.3 Integrated intensity vs stress – deformation induced transformations

The evolution of the normalized integrated intensities of different grain families is shown in Figure 5. Within the range of experimental error, the integrated intensities for all grain orientations do not exhibit values (significantly) above their initial values, i.e. the normalized integrated intensities never grew significantly above 1. Instead, all grain orientations show a significant decrease of the normalized integrated intensities. This decrease is explained by the forward phase transformation fcc→hcp. An increase of the normalized integrated intensity above 1 would likely be caused by the formation of a deformation texture, however all diffraction peak intensities decrease (during tension), indicating that the phase transformation superimposes the texture effect. This allows associating, semi-quantitatively, the changes of the integrated intensities to the fcc ↔ hcp phase transformation. During forward phase transformation, the integrated intensity for a specific austenitic grain family decreases while at the same time the hcp volume fraction increases. On the other hand, an increase of the integrated intensity of an austenite peak is explained by the reverse transformation hcp→fcc. In this case, the fcc volume fraction of a certain grain family is growing at the expense of the hcp phase fraction.

During tensile loading (from 0 MPa to 560 MPa, corresponding to 0% to +2% strain) the integrated intensities of the {111}, {200}, {220}, {331} and {420} grain families decrease. This decrease of integrated intensity is a result of the fcc→hcp transformation. Even though for the {200} and {420} grain families the SF of the leading partial dislocation is smaller or equal to the SF of the trailing partial dislocation (PYES grains), these two grain families undergo a fcc→hcp transformation upon tensile stress. For the PYES grains, less nucleation sites for the hcp phase will be available upon tension, however the partial dislocations can still nucleate from the grain boundaries and move into the material to develop hcp plates.

Upon compression from +2%→-2% (560 MPa to -590 MPa), an increase of the normalized integrated intensity is observed for the {220}, {331} and {111} grains. This can be explained by the reverse hcp→fcc phase transformation. This phase reversion is predominant until around -360 MPa (0% strain). At this stress, the integrated intensity shows a maximum turning point. For compressive stresses larger than -360 MPa, the integrated intensity decreases, which indicates a fcc→hcp forward phase transformation in the last stage of compression. Therefore, two different deformation mechanisms are identified in the compressive region for the {220}, {331} and {111} grain families: phase reversion (hcp→fcc) first and then forward phase transformation (fcc→hcp).

The {311} grain family is identified as the only grain family for which the intensity at +2% does not change significantly. The {311} grain family shows an increase of the FWHM to 0.025 \AA^{-1} during straining to 560 MPa and a decrease of the FWHM to 0.012 \AA^{-1} during subsequent compression as can be seen in Figure 4 e). The reversible behavior of the FWHM during tension-compression can be explained by the reversible movement of the partial dislocations. For the {311} grain families the partial dislocations do not form the hcp phase during tension to 560 MPa, which is concluded from the absence of a decrease of integrated intensity at 560 MPa. A phase transformation from fcc→hcp is observed for the {311} grain families at the end of the cycle for compressive stresses during the increase

of the compressive stress from -440 MPa to -590 MPa where the integrated intensity significantly decreases from -5% to -13%. It is expected that the {311} grain family would also transform to hcp for tensile strains, but probably at a higher stress than +560 MPa.

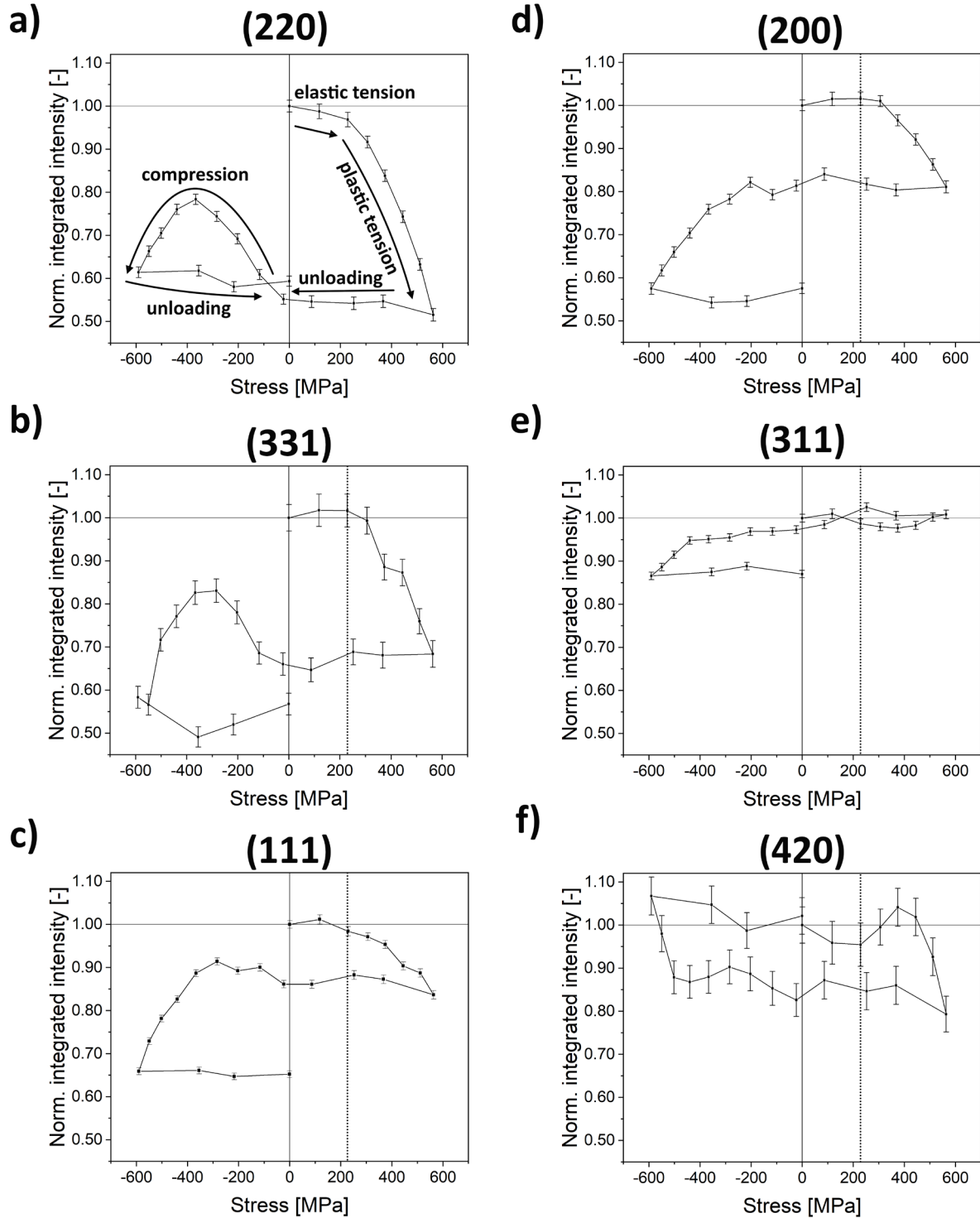


Figure 5: Changes of integrated intensities for various grain families in the course of straining from 0%→+2% (560 MPa)→-2% (-590 MPa) → unloading. a), b) and c) show PYEC grains exhibiting a phase reversion upon compression. d) and e) show PYES grains without phase reversion. f) The {420} grain family behaves PYES and shows a minor phase reversion upon compression.

3.3 Electron backscatter diffraction – Disappearance and thickening of bands

Quasi *in situ* EBSD investigation was done to complement the neutron diffraction experiments. A selected $\langle 541 \rangle$ orientated grain with respect to the loading direction, with a high SF for the $\{111\}\langle 112 \rangle$ slip system in tension, 0.49, and a low SF in compression, 0.31, is shown in Figure 6 a) and b). These SF are associated with the $[-1-11]$ plane, which is the active slip plane (cf. supplementary table). The $\langle 541 \rangle$ grain orientation was selected from the EBSD map since it possesses a close orientation to the $\{220\}$ grain family and therefore a similar behavior is expected (Figure 6 e)).

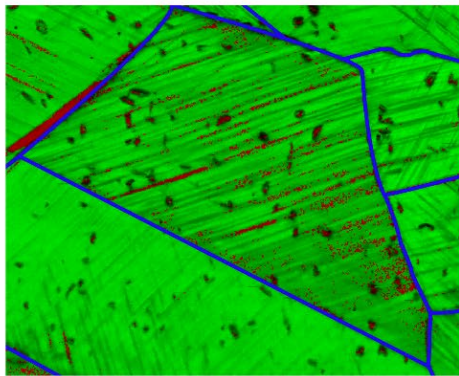
In Figure 6 c) and d) a $\langle 200 \rangle$ orientated grain with respect to the loading direction, with a low Schmid of 0.24 under tension and a high SF of 0.47 under compression, is shown. For the $\{200\}$ grain families all twelve $\{111\}\langle 112 \rangle$ slip systems have the same SF (Supplementary table). Thus, these two grain orientations, $\langle 541 \rangle$ and $\langle 200 \rangle$, represent two different SF sequences: high SF (tension) \rightarrow low SF (compression) and, low SF (tension) \rightarrow high SF (compression), respectively. Thus, the $\langle 541 \rangle$ orientated grain represents a PYEC grain and the $\langle 200 \rangle$ orientated grain represents a PYES grain.

The phase maps shown in Figure 6 are overlaid with the EBSD image quality maps. While the image quality maps show grey bands, these bands are not always indexed as the hcp phase. It is expected that these bands contain a mixture of hcp plates embedded in a fcc matrix as observed by TEM measurements by Kikuchi et. al [44]. It is important to know that for the EBSD conditions used in the present study (20 kV, 70° tilt, iron-based sample) the probing volume of the electrons with the material is in the range of ~ 50 nm for a single EBSD data point. If several phases are present within the probing volume, in this case fcc and hcp, it is likely that the phase with the strongest diffraction contrast dominates the Kikuchi pattern. Therefore, it is expected that the bands that are not indexed as hcp contain a mixture of fcc and hcp. However, the fcc phase is still dominant in these bands. For bands which appear as the hcp phase (red), this phase is more dominant over the fcc phase (green).

For the $\langle 541 \rangle$ orientated grain a phase reversion is observed; on the top and in the bottom parts of the grains less hcp bands are visible at $0\% \rightarrow +2\% \rightarrow -2\% \rightarrow$ unloading when compared to the visible hcp plates at $0\% \rightarrow +2\% \rightarrow$ unloading (Figure 6 a) and b)). This is in agreement with the analysis of the integrated intensities where an increase of the integrated intensity is observed during compression for the similarly orientated $\{220\}$ grain family, which was explained by the growth of the fcc phase due to the reverse transformation $\text{hcp} \rightarrow \text{fcc}$.

Based on the integrated intensities upon compression no phase reversion is expected for the $\{200\}$ grain family. Indeed, the EBSD map of the $\langle 200 \rangle$ orientated grain shown in Figure 6 c) and d) does not indicate any disappearance of hcp bands upon compression, but thickening of the bands.

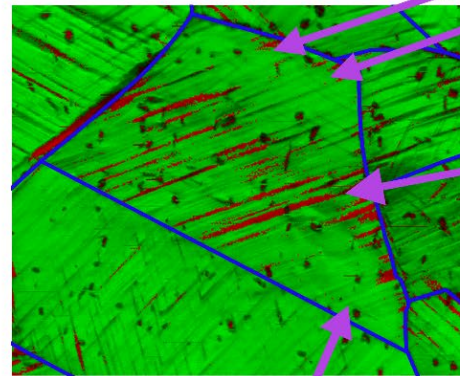
a) green: fcc, red: hcp
0→+2%→unloading,
<541>



30 μm



b) 0%→2+%→-2%→ unloading,
<541>

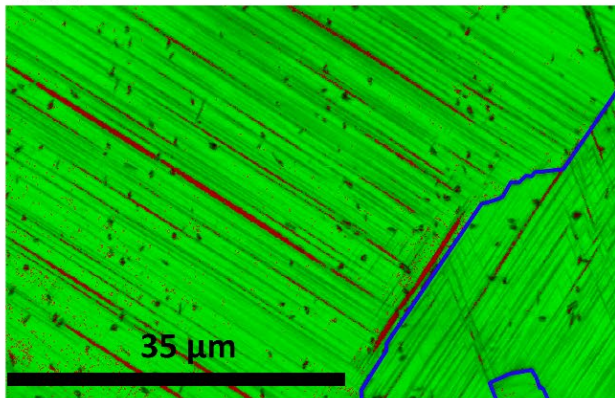


phase reversion

phase reversion

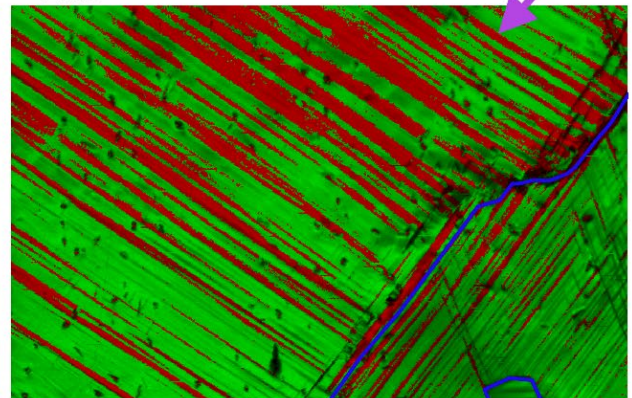
thickening

c) 0→+2%→unloading,
<200>



35 μm

d) 0%→2+%→-2%→ unloading,
<200>



thickening

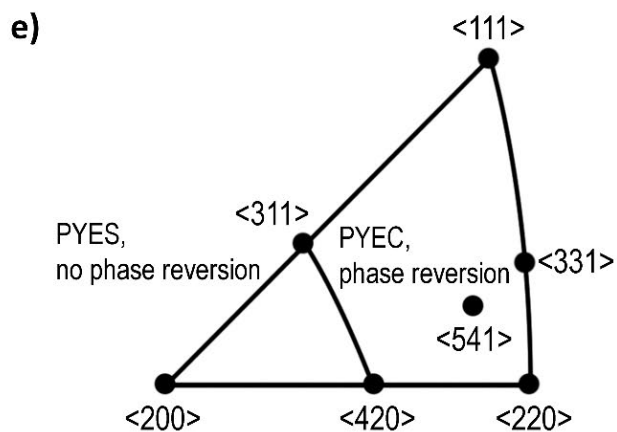


Figure 6: Phase maps overlaid with image quality maps at two different strains for two different grain orientations. The blue lines indicate grain boundaries. In a) and b) a PYEC <541> orientated grain is shown, while c) and d) show a PYES <200> orientated grain. e) Inverse pole figure representing all grain directions studied by EBSD and neutron diffraction.

3.4 Phase reversion vs. forward phase transformation

During tensile straining to +2%, the hcp variant with the highest SF preferentially forms and the parent grains show parallel bands containing hcp variants with the same crystallographic orientation. The formation of single variant hcp was already observed in another study for FeMnSi at strains $< +2\%$ [45].

Upon subsequent compression, two possible mechanisms are observed: phase reversion of the martensite that formed under tension or new phase transformation due to compression. For the phase reversion the same slip system is active under compression as under tension, while the direction of slip is reversed. Hence, the SF for martensite formation under tension is the same as for the martensite reversion under compression. It is observed that the SF for martensite formation under tension (and subsequent reversion under compression) is higher than the SF for martensite formation under compression, for the {220}, {331} and {111} grain families. Hence, phase reversion is more favorable than new martensite formation under compression in these grain families. It was shown that these three grain families behaved PYEC based on the analysis of the elastic lattice strain. The elastic lattice strain indicates a compliant behavior for these three grain families in the compressive region in the range between 0 MPa to -300 to -400 MPa. The elastically compliant behavior is the consequence of the phase reversion $\text{hcp} \rightarrow \text{fcc}$.

In contrast, the {200} grain family does not exhibit phase reversion upon compression. For this grain family, the SF for martensite formation under tension (and subsequent reversion under compression) is 0.24, whereas the SF for martensite formation upon compression is 0.47. Therefore, the {200} grain family exhibits activation of a new slip system upon compression, and subsequent formation of new martensite, which is more favorable than the reversion of hcp variants that formed under tension. The latter interpretation is supported by the EBSD characterization shown in Figure 6 c) and d) and the evolution of the integrated intensities for the {200} grain family shown in Figure 5. We conclude that grains with the SF sequence for martensite formation high (tension) \rightarrow low (compression) will undergo a phase reversion upon compression, while no phase reversion is expected for grains with the SF sequence for martensite formation of low (tension) \rightarrow high (compression). A schematic for the phase transformations occurring for both of these SF sequences is shown in Figure 7.

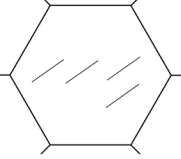
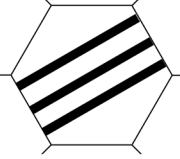
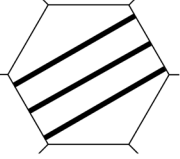
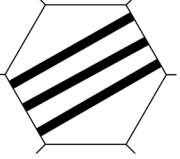
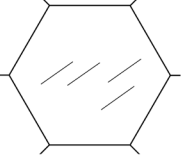
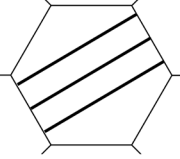
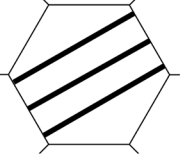
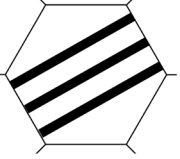
	0% 0 MPa unstrained	+2% +560 MPa Tension	0% -370 MPa Compression	-2% -590 MPa Compression
<541> orientated grain, {220} and {331} grain families	 No hcp, but stacking faults expected	 Activation of first slip system, Schmid factor 0.49	 Partial reversion of first slip system, Schmid factor 0.49	 Activation of second slip system on same plane, Schmid factor 0.31
<200> orientated grain, {200} grain family	 No hcp, but stacking faults expected	 Activation of first slip system, Schmid factor 0.24	 Activation of second slip system on same plane, Schmid factor 0.47	 Second slip system still active, Schmid factor 0.47

Figure 7: Schematic illustrating the phase transformations at different strains for two different grain orientations and different grain families. The thickness of a band represents the amount of hcp phase in each grain. While the <541> orientated grain shows a phase reversion upon compression, the <200> orientated grain does not show a phase reversion. During the whole deformation cycle two different slip systems are active on the same plane creating single variant hcp martensite.

<541> and <200> orientated grains show hcp bands at both strains 0%→+2%→unloading and 0%→+2%→-2%→unloading. The single variant martensite bands are parallel to each other in each grain. For both grain orientations the bands which have formed during tension are thinner than the width of the bands after compression, not considering the bands which disappeared for the <541> orientated grain. It is assumed that during compression thin martensite plates nucleate and coalesce with existing martensite bands formed under tension which leads to the thickening of the existing bands. The mechanism of formation of thin plates and the clustering of plates to form larger bands is a mechanism observed for FeMnSi [44,46] or thermally induced fcc-hcp phase transformations in Cu alloys [47]. The thickening of bands in the current tension-compression cycle is therefore similar to the thickening of bands during sole tension.

For the <541> and <200> orientated grains the two slip systems with the maximum SF for martensite formation under tension and compression are on the same {111} plane, i.e. ($\bar{1}\bar{1}1$) (see "Plane 4" in the supplementary table), however slip occurs along two different slip direction. Since the same slip plane is involved in the martensitic transformation upon tension and compression, new plates form with the same crystallographic orientation, which is seen as thickening of the bands which formed under tension (Figure 6).

			Tension {111}<112>		Compression {111}<112>	
Grain family	PYEC or PYES	Phase Re-version	HCP formation	SF	HCP formation	SF
{111}	PYEC	Yes	Small	0.31	Medium	0.16
{220}	PYEC	Yes	Large	0.47	Small	0.24
{331}	PYEC	Yes	Large	0.50	Small	0.25
{200}	PYES	No	Small	0.24	Large	0.47
{311}	PYES	No	No	0.39	Small	0.39
{420}	PYES	Yes (minor)	Small	0.42	No	0.42

Table 1: Summary of the micro-mechanical behavior and the SF of the different grain families.

Conclusions

The grain orientation dependent phase transformation behavior of a precipitate containing FeMnSi-based shape memory alloy was studied by *in situ* neutron diffraction and quasi *in situ* EBSD characterization for the load cycle $0\% \rightarrow +2\% \rightarrow -2\% \rightarrow \text{unloading}$. The following conclusions can be drawn:

- i) A deformation-induced fcc \rightarrow hcp transformation was observed for all grain families. For most of the grains solely one main slip plane was active.
- ii) Grains behave PYEC under tension when the SF of the leading partial dislocation is larger than the SF of the trailing partial dislocation. Grains behave PYES when the opposite is true. Based on the grain orientation the width of pre-existing stacking faults increases or decreases and thus facilitates (PYEC) or inhibits (PYES) the nucleation and growth of the hcp phase.
- iii) A phase reversion upon compression was observed for grains where the SF for tension is larger than the SF for compression.
- iv) The micro-mechanical behavior of a grain family can be predicted based on its SF sequence: i) PYEC + phase reverting grains: high SF (tension) \rightarrow low SF (compression) and ii) PYES + not phase reverting grain: low SF (tension) \rightarrow high SF (compression).
- v) A thickening of the hcp bands which form during tension is observed during subsequent compression. It is suggested that the thickening of bands during compression is caused by a slip system which is different than the slip system active during tension, but acting on the same slip plane.
- vi) The FWHM is an indicator of the defect density. The defect density decreases upon compression for all grain families. The decrease can be explained by the reversible movement of partial dislocations and by the reverse transformation from hcp to fcc.

The current results give insights into the grain orientation dependent plastic behavior during cyclic loading. Since FeMnSi-based shape memory alloys are used for engineering applications where the material usually undergoes both tensile and compressive stresses, the current results are valuable for improving the functionality and open new perspectives for tailoring their microstructure to meet the need of the application. Moreover, the current study reveals fundamental insights into the plastic deformation mechanism during cyclic loading for materials exhibiting a fcc \leftrightarrow hcp transformation.

Acknowledgement

The financial support by the Swiss National Science Foundation (SNSF grant No. [200021_150109/1](#)) as well as by the company re-Fer AG, Wollerau, Switzerland, is gratefully acknowledged. M. Smid thanks the European Research Council for financial support within the ERC-advanced grant MULTIAX (339245).

Data availability statement

The data that support the findings of this study are available from the corresponding author on reasonable request.

Declaration of competing interest

All authors declare that they have no competing interest for this publication.

References

- [1] A. Sato, E. Chishima, Y. Yamaji, T. Mori, Orientation and composition dependencies of shape memory effect in Fe-Mn-Si alloys, *Acta Metallurgica*. 32 (1984) 539–547. [https://doi.org/10.1016/0001-6160\(84\)90065-8](https://doi.org/10.1016/0001-6160(84)90065-8).
- [2] A. Sato, K. Soma, E. Chishima, T. Mori, Shape memory effect and mechanical behaviour of an Fe-39Mn-1Si alloy single crystal, *Le Journal de Physique Colloques*. 43 (1982) 797–802. <https://doi.org/10.1051/jphyscol:19824130>.
- [3] K. Sato, M. Ichinose, Y. Hirotsu, Y. Inoue, Effects of deformation induced phase transformation and twinning on the mechanical properties of austenitic Fe-Mn-Al alloys, *ISIJ International*. 29 (1989) 868–877. <https://doi.org/10.2355/isijinternational.29.868>.
- [4] P. Behjati, A. Najafizadeh, Role of chemical driving force in martensitic transformations of high-purity Fe-Cr-Ni Alloys, *Metallurgical and Materials Transactions A*. 42 (2011) 3752–3760. <https://doi.org/10.1007/s11661-011-0769-x>.
- [5] S. Martin, S. Wolf, U. Martin, L. Krüger, D. Rafaja, Deformation mechanisms in austenitic TRIP/TWIP steel as a function of temperature, *Metallurgical and Materials Transactions A*. 47 (2014) 49–58. <https://doi.org/10.1007/s11661-014-2684-4>.
- [6] N. Gey, B. Petit, M. Humbert, Electron backscattered diffraction study of ϵ/α' martensitic variants induced by plastic deformation in 304 stainless steel, *Metallurgical and Materials Transactions A*. 36 (2005) 3291–3299. <https://doi.org/10.1007/s11661-005-0003-9>.
- [7] E. Polatidis, W.N. Hsu, M. Šmíd, T. Panzner, S. Chakrabarty, P. Pant, H. Van Swygenhoven, Suppressed martensitic transformation under biaxial loading in low stacking fault energy metastable austenitic steels, *Scripta Materialia*. 147 (2018) 27–32. <https://doi.org/10.1016/j.scriptamat.2017.12.026>.
- [8] H. Otsuka, H. Yamada, T. Maruyama, H. Tanahashi, S. Matsuda, M. Murakami, Effects of alloying additions on Fe-Mn-Si shape memory alloys, *ISIJ International*. 30 (1990) 674–679. <https://doi.org/10.2355/isijinternational.30.674>.
- [9] N. Stanford, D.P. Dunne, Thermo-mechanical processing and the shape memory effect in an Fe-Mn-Si-based shape memory alloy, *Materials Science and Engineering: A*. 422 (2006) 352–359. <https://doi.org/10.1016/j.msea.2006.02.009>.
- [10] C.Y. Chung, C. Shuchuan, T.Y. Hsu, Thermomechanical training behavior and its dynamic mechanical analysis in an Fe-Mn-Si shape memory alloy, *Materials Characterization*. 37 (1996) 227–236. [https://doi.org/10.1016/s1044-5803\(96\)00149-0](https://doi.org/10.1016/s1044-5803(96)00149-0).
- [11] S. Kajiwarra, D. Liu, T. Kikuchi, N. Shinya, Remarkable improvement of shape memory effect in Fe-Mn-Si based shape memory alloys by producing NbC precipitates, *Scripta Materialia*. 44 (2001) 2809–2814. [https://doi.org/10.1016/s1359-6462\(01\)00978-2](https://doi.org/10.1016/s1359-6462(01)00978-2).
- [12] M. Shahverdi, C. Czaderski, M. Motavalli, Iron-based shape memory alloys for prestressed near-surface mounted strengthening of reinforced concrete beams, *Construction and Building Materials*. 112 (2016) 28–38. <https://doi.org/10.1016/j.conbuildmat.2016.02.174>.
- [13] C. Leinenbach, H. Kramer, C. Bernhard, D. Eifler, Thermo-mechanical properties of an Fe-Mn-Si-Cr-Ni-VC shape memory alloy with low transformation temperature, *Advanced Engineering Materials*. 14 (2012) 62–67. <https://doi.org/10.1002/adem.201100129>.
- [14] W.J. Lee, B. Weber, C. Leinenbach, Recovery stress formation in a restrained Fe-Mn-Si-based shape memory alloy used for prestressing or mechanical joining, *Construction and Building Materials*. 95 (2015) 600–610. <https://doi.org/10.1016/j.conbuildmat.2015.07.098>.
- [15] P. Dai, L. Zhou, Investigation on the connecting strength of Fe-Mn-Si-C shape memory alloy pipe coupling, *Journal of Materials Science*. 41 (2006) 3441–3443. <https://doi.org/10.1007/s10853-006-7933-5>.

- [16] A.V. Druker, A. Perotti, I. Esquivel, J. Malarría, A manufacturing process for shaft and pipe couplings of Fe–Mn–Si–Ni–Cr shape memory alloys, *Materials & Design* (1980–2015). 56 (2014) 878–888. <https://doi.org/10.1016/j.matdes.2013.11.032>.
- [17] T. Sawaguchi, P. Sahu, T. Kikuchi, K. Ogawa, S. Kajiwara, A. Kushibe, M. Higashino, T. Ogawa, Vibration mitigation by the reversible fcc/hcp martensitic transformation during cyclic tension–compression loading of an Fe–Mn–Si-based shape memory alloy, *Scripta Materialia*. 54 (2006) 1885–1890. <https://doi.org/10.1016/j.scriptamat.2006.02.013>.
- [18] O.E. Ozbulut, S. Hurlbaas, R. Desroches, Seismic response control using shape memory alloys: A review, *Journal of Intelligent Material Systems and Structures*. 22 (2011) 1531–1549. <https://doi.org/10.1177/1045389x11411220>.
- [19] Y.-B. Ju, M. Koyama, T. Sawaguchi, K. Tsuzaki, H. Noguchi, Effects of ϵ -martensitic transformation on crack tip deformation, plastic damage accumulation, and slip plane cracking associated with low-cycle fatigue crack growth, *International Journal of Fatigue*. 103 (2017) 533–545. <https://doi.org/10.1016/j.ijfatigue.2017.06.040>.
- [20] T. Sawaguchi, I. Nikulin, K. Ogawa, K. Sekido, S. Takamori, T. Maruyama, Y. Chiba, A. Kushibe, Y. Inoue, K. Tsuzaki, Designing Fe–Mn–Si alloys with improved low-cycle fatigue lives, *Scripta Materialia*. 99 (2015) 49–52. <https://doi.org/10.1016/j.scriptamat.2014.11.024>.
- [21] I. Nikulin, T. Sawaguchi, K. Tsuzaki, Effect of alloying composition on low-cycle fatigue properties and microstructure of Fe–30Mn–(6–x)Si–xAl TRIP/TWIP alloys, *Materials Science and Engineering: A*. 587 (2013) 192–200. <https://doi.org/10.1016/j.msea.2013.08.061>.
- [22] I. Nikulin, T. Sawaguchi, K. Ogawa, K. Tsuzaki, Effect of γ to ϵ martensitic transformation on low-cycle fatigue behaviour and fatigue microstructure of Fe–15Mn–10Cr–8Ni–x Si austenitic alloys, *Acta Materialia*. 105 (2016) 207–218. <https://doi.org/10.1016/j.actamat.2015.12.002>.
- [23] M.J. Szczerba, S. Kopacz, M.S. Szczerba, Experimental studies on detwinning of face-centered cubic deformation twins, *Acta Materialia*. 104 (2016) 52–61. <https://doi.org/10.1016/j.actamat.2015.11.025>.
- [24] Q. Xie, Y. Chen, P. Yang, Z. Zhao, Y.D. Wang, K. An, In-situ neutron diffraction investigation on twinning/detwinning activities during tension-compression load reversal in a twinning induced plasticity steel, *Scripta Materialia*. 150 (2018) 168–172. <https://doi.org/10.1016/j.scriptamat.2018.03.017>.
- [25] T. Sawaguchi, L.-G. Bujoreanu, T. Kikuchi, K. Ogawa, M. Koyama, M. Murakami, Mechanism of reversible transformation-induced plasticity of Fe–Mn–Si shape memory alloys, *Scripta Materialia*. 59 (2008) 826–829. <https://doi.org/10.1016/j.scriptamat.2008.06.030>.
- [26] C. Leinenbach, A. Arabi-Hashemi, W.J. Lee, A. Lis, M. Sadegh-Ahmadi, S. Van Petegem, T. Panzner, H. Van Swygenhoven, Characterization of the deformation and phase transformation behavior of VC-free and VC-containing FeMnSi-based shape memory alloys by in situ neutron diffraction, *Materials Science and Engineering: A*. 703 (2017) 314–323. <https://doi.org/10.1016/j.msea.2017.07.077>.
- [27] S. Lee, J. Im, Y. Yoo, E. Bitzek, D. Kiener, G. Richter, B. Kim, S.H. Oh, Reversible cyclic deformation mechanism of gold nanowires by twinning-detwinning transition evidenced from in situ TEM, *Nature Communications*. 5 (2014) 3033. <https://doi.org/10.1038/ncomms4033>.
- [28] S. Martin, C. Ullrich, D. Rafaja, Deformation of austenitic CrMnNi TRIP/TWIP steels: nature and role of the ϵ -martensite, *Materials Today: Proceedings*. 2 (2015) 643–646. <https://doi.org/10.1016/j.matpr.2015.07.366>.
- [29] E. Polatidis, M. Šmíd, W.-N. Hsu, M. Kubenova, J. Capek, T. Panzner, H. Van Swygenhoven, The interplay between deformation mechanisms in austenitic 304 steel during uniaxial and equibiaxial loading, *Materials Science and Engineering: A*. 764 (2019) 138222. <https://doi.org/10.1016/j.msea.2019.138222>.

- [30] A. Sato, Y. Sunaga, T. Mori, Contribution of the $\gamma \rightarrow \epsilon$ transformation to the plastic deformation of stainless steel single crystals, *Acta Metallurgica*. 25 (1977) 627–634. [https://doi.org/10.1016/0001-6160\(77\)90004-9](https://doi.org/10.1016/0001-6160(77)90004-9).
- [31] Y. Tomota, S. Harjo, P. Lukáš, D. Neov, P. Šittner, In-situ neutron diffraction during shape-memory behavior in Fe–Mn–Si–Cr, *Journal of Materials*. 52 (2000) 32–34. <https://doi.org/10.1007/s11837-000-0080-6>.
- [32] J. Martínez, G. Aurelio, G.J. Cuello, S.M. Cotes, J. Desimoni, Structural properties of fcc and hcp phases in the Fe–Mn–Si system: A neutron diffraction experiment, *Materials Science and Engineering: A*. 437 (2006) 323–327. <https://doi.org/10.1016/j.msea.2006.08.014>.
- [33] E.C. Oliver, T. Mori, M.R. Daymond, P.J. Withers, Comparison using neutron diffraction of martensitic transformation in Fe–Mn–Si shape memory alloys with and without VN precipitates, *Materials Science and Technology*. 24 (2013) 902–907. <https://doi.org/10.1179/174328408x302576>.
- [34] U. Stuhr, Time-of-flight diffraction with multiple pulse overlap. Part I: The concept, *Nuclear Instruments and Methods in Physics Research Section A: Accelerators, Spectrometers, Detectors and Associated Equipment*. 545 (2005) 319–329. <https://doi.org/10.1016/j.nima.2005.01.320>.
- [35] U. Stuhr, H. Spitzer, J. Egger, A. Hofer, P. Rasmussen, D. Graf, A. Bollhalder, M. Schild, G. Bauer, W. Wagner, Time-of-flight diffraction with multiple frame overlap Part II: The strain scanner POLDI at PSI, *Nuclear Instruments and Methods in Physics Research Section A: Accelerators, Spectrometers, Detectors and Associated Equipment*. 545 (2005) 330–338. <https://doi.org/10.1016/j.nima.2005.01.321>.
- [36] O. Arnold, J.C. Bilheux, J.M. Borreguero, A. Buts, S.I. Campbell, L. Chapon, M. Doucet, N. Draper, R. Ferraz Leal, M.A. Gigg, V.E. Lynch, A. Markvardsen, D.J. Mikkelsen, R.L. Mikkelsen, R. Miller, K. Palmen, P. Parker, G. Passos, T.G. Perring, P.F. Peterson, S. Ren, M.A. Reuter, A.T. Savici, J.W. Taylor, R.J. Taylor, R. Tolchenov, W. Zhou, J. Zikovsky, Mantid-Data analysis and visualization package for neutron scattering and μ SR experiments, *Nuclear Instruments and Methods in Physics Research Section A: Accelerators, Spectrometers, Detectors and Associated Equipment*. 764 (2014) 156–166. <https://doi.org/10.1016/j.nima.2014.07.029>.
- [37] N. Stanford, D.P. Dunne, H. Li, Re-examination of the effect of NbC precipitation on shape memory in Fe–Mn–Si-based alloys, *Scripta Materialia*. 58 (2008) 583–586. <https://doi.org/10.1016/j.scriptamat.2007.11.018>.
- [38] M.J. Lai, Y.J. Li, L. Lillpopp, D. Ponge, S. Will, D. Raabe, On the origin of the improvement of shape memory effect by precipitating VC in Fe–Mn–Si-based shape memory alloys, *Acta Materialia*. 155 (2018) 222–235. <https://doi.org/10.1016/j.actamat.2018.06.008>.
- [39] A. Sato, T. Mori, Development of a shape memory alloy Fe–Mn–Si, *Materials Science and Engineering: A*. 146 (1991) 197–204. [https://doi.org/10.1016/0921-5093\(91\)90277-t](https://doi.org/10.1016/0921-5093(91)90277-t).
- [40] W.G. Burgers, J.A. Klostermann, Influence of the direction of deformation on the transition of austenite into martensite, *Acta Metallurgica*. 13 (1965) 568–572. [https://doi.org/10.1016/0001-6160\(65\)90114-8](https://doi.org/10.1016/0001-6160(65)90114-8).
- [41] S. Kibey, J.B. Liu, D.D. Johnson, H. Sehitoglu, Energy pathways and directionality in deformation twinning, *Applied Physics Letters*. 91 (2007) 181916. <https://doi.org/10.1063/1.2800806>.
- [42] T.S. Byun, On the stress dependence of partial dislocation separation and deformation microstructure in austenitic stainless steels, *Acta Materialia*. 51 (2003) 3063–3071. [https://doi.org/10.1016/s1359-6454\(03\)00117-4](https://doi.org/10.1016/s1359-6454(03)00117-4).
- [43] B. Jiang, T. Tadaki, H. Mori, T.Y. Hsu Xu Zuyao, In-situ TEM observation of gamma to epsilon martensitic transformation during tensile straining in an FeMnSi shape memory alloy, *Mater. Trans., JIM*. 38 (1997) 1072–1077. <https://doi.org/10.2320/matertrans1989.38.1072>.
- [44] T. Kikuchi, S. Kajiwara, Y. Tomota, Microscopic studies on stress-induced martensite transformation and its reversion in an Fe–Mn–Si–Cr–Ni shape memory alloy, *Materials Transactions, JIM*. 36 (1995) 719–728. <https://doi.org/10.2320/matertrans1989.36.719>.

- [45] B.C. Maji, M. Krishnan, The effect of microstructure on the shape recovery of a Fe–Mn–Si–Cr–Ni stainless steel shape memory alloy, *Scripta Materialia*. 48 (2003) 71–77.
[https://doi.org/10.1016/s1359-6462\(02\)00348-2](https://doi.org/10.1016/s1359-6462(02)00348-2).
- [46] T. Kikuchi, S. Kajiwara, Y. Tomota, Formation Process of Lamella Structures by Deformation in an Fe-Mn-Si-Cr-Ni Shape Memory Alloy, *Le Journal de Physique IV*. 05 (1995) 445–450.
<https://doi.org/10.1051/jp4:1995867>.
- [47] E. Polatidis, N. Zotov, E. Bischoff, E.J. Mittemeijer, Kinetics of the fcc → hcp Phase transformation in Cu-Ge solid solutions upon isothermal aging, *Metallurgical and Materials Transactions A*. 48 (2017) 5304–5316. <https://doi.org/10.1007/s11661-017-4319-z>.